# A Computational Fluid Dynamics Study of a 2D Airfoil in Hovering Flight Under Ground Effect

**J.M.C.Pereira[1], N.A.R.Maia [1] and J.C.F.Pereira[1]**

**Abstract:**    We present a 2D incompressible Navier-Stokes numerical simulation of a virtual model of an elliptic, or flat plate, foil in hovering flight configuration. Computations obtained with a general purpose solver were validated against reference data on forward flapping flight, normal or dragonfly hovering. The moving mesh technique allows airfoil translation and angular mesh movement accompaining the airfoil stroke motion. Close to the ground the mesh deforms to occupy the narrow computational domain formed between the airfoil and the ground. Computations have been carried out for some parameters, including the distances $h$ between the foil center and the surface, $h/c = \infty$, 1.5 and 1.0, for chord Reynolds numbers of 157, 1570 and 3140. The combination of the selected parameters showed force reduction and force recovery to the free dragonfly mode. During the first stroke, lift is dominated by leading edge vortex and wake capture. With the number of strokes increasing, the interactions between the airfoil and the regions related to the previous stroke vortices and the vortices emanating from the boundary layer on ground growth, and the drag and lift temporal evolution do not show a periodic behavior with the stroke motion.

**Keywords:**    Dragonfly hovering; Insect flight; Ground effect; Vortices.

**Nomenclature**

**Latin:**

$A_0$ - Stroke amplitude

$c$ - Chord

$f$ - Flap frequency

$h$ - Distance from the profile's center to the ground

$\vec{u_{bd}}$ - Velocity at the boundary

---

[1] Instituto Superior Técnico, Technical University of Lisbon, Av. Rovisco Pais, 1, 1049-001, Lisbon, Portugal

$\vec{u}_{tr}$ - Translational Velocity

$\vec{r}$ - Vertex position

$T$ - Stroke period

$U_0$ - Reference velocity

$x(t)$ - Translational position

**Greek:**

$\alpha_0$ - Initial angle of attack

$\alpha_1$ - Amplitude of pitching angle of attack

$\alpha(t)$ - Angle of attack

$\beta$ - Angle of motion line

$\vec{\omega}$ - Angular velocity

$\phi$ - Phase angle between $x(t)$ and $\alpha(t)$

$\nu$ - Viscosity

**Non-dimensional numbers:**

Reynolds number - $Re = U_0 c / \nu$

Strouhal number (translational movement related) - $St_a = f A_0 / U_0$

Strouhal number (rotational movement related - pitching) - $St_c = f c / U_0$

## 1   Introduction

Recently interest has been growing in studying insect flight and applying its knowledge to the development of micro air vehicles (MAV) that may be used for surveillance, search and rescue operations. The mimic of insect flight, and in particular hovering flight, could inspire very successful MAVs design because of the superior unsteady aerodynamic performance of flapping flight compared with conventional wings and rotors, see e.g., Sane (2003), Van den Berg and Ellington (1997a) and Shyy, Berg, and Ljungqvist (1999).

The scientific interest for flapping flight has documented history dating back to the nineteenth century. Marey (1868) filmed and also traced wing motion characteristics and since then cameras have revealed 3D wing motion details.

Measurements of the instantaneous aerodynamic forces on a live insect are still a challenge to the scientific community, see e.g., Hollick (1940), Jensen (1956), Nachtigall (1974) or Wang, Zeng, Liu, and Yin (2003). Studies reporting mechanical, wings scaled up from insects, have been investigated for the hawkmoth insect, for example by Ellington, van den Berg, Willmott, and Thomas (1996) while for
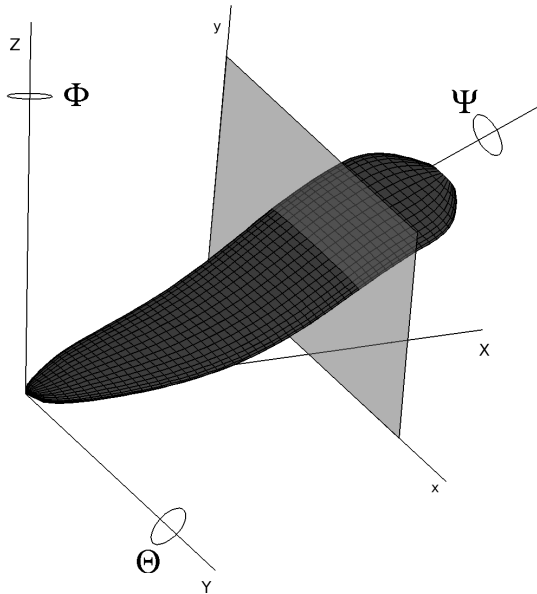
Figure 1: 2D slice from a full 3D model.

the insect fruit fly (Drosophilia Melanogaster) by Dickinson, Lehmann, and Sane (1999). Studies focusing on the unsteady flow and forces on flapping wings at Reynolds number in between 10 to $10^4$ have been reported, see the reviews, e.g. Ellington (1999), Sane (2003), Wang (2005) and Ho, Nassef, Pornsinsirirak, Tai, and Ho (2003).

A large amount of knowledge has been collected since the Weis-Fogh (1973) and Lighthill (1973) and later Maxworthy (1979) have explained the fluid-dynamic processes that allow certain insects to generate large lift coefficients in hovering flight with the so-called 'clap and fling' mechanism. Experiments have verified that the leading edge vortex (LEV) plays an important role in insect flight to significantly generate lift during the translation of the flapping wing, see, for example, Dickinson and Götz (1993), Ellington, van den Berg, Willmott, and Thomas (1996), Birch and Dickinson (2001).

Apart from the LEV the insect flight performance depends also on the way the wing interacts with its wake and with the shed vortices. This fact is even more relevant during hovering, because the wing-wake interaction is more emphasized than in forward flight. The complex interaction between the wing and its wake

is an aerodynamic characteristic of the insect flapping flight and any successful aerodynamic model must be able to capture this complex interactions, see Van den Berg and Ellington (1997b) and Lehmann (2008).

Insects do most of the flight modes near surfaces and MAVs are expected to hover in surfaces vicinity like some insects do. A key difference between normal and inclined, dragonfly, stroke plane hovering is that almost all the aerodynamic force is produced on the downstroke in the later. Consequently the insect will have to use unsteady lift enhancing mechanisms with huge power demands during the downstroke.

In the present study the dragonfly hovering flight was also studied under the ground influence with a minimum clearance distance of one chord (between the ground level and the airfoil center), being that the trailing edge is located closest to the ground.

If the lift force is increased under ground influence the power can be substantially reduced. This effect occurs through interaction between the vortex wake of the flying animal and an underlying physical surface. Upwash from the surface reduces the downward momentum flux required to offset the body weight and the ground effect should manifest its effectiveness in hovering flight when induced velocities are highest.

During the course of this work the ground effect influence on the dragonfly normal hovering flapping wing aerodynamics was considered by Gao and Lu (2008) for low Reynolds number $Re = 100$ and in normal hovering flight, without vertical translational airfoil motion. When the ground clearance increases, the mean vertical force decreases quickly to a minimum, then increases gradually and approaches the value without ground effect. The regimes were identified and closely associated with the evolution of the vortex structures. This interesting study should be extended to investigate if the same conclusions can be withdrawn for higher Strouhal and Reynolds numbers.

The main objective of the present study is to predict the flapping dragonfly hovering characteristics under ground effect. The same kinematics as in free flight mode were kept.

Numerical solutions of the Navier-Stokes equations for a moving wing section have been obtained using several numerical techniques: the method of artificial compressibility (Liu, Ellington, Kawachi, van den Berg, and Willmott (1998), Sun and Tang (2002)), the finite element method (Ramamurti and Sandberg (2002) and Yamada and Yoshimura (2008)), the immersed boundary method (Miller and Peskin (2004)), the vortex particle method by Eldredge (2005), the boundary element method (La Mantia and Dabnichki (2008)) and the immersed boundary Lat-

tice Boltzmann method, Gao and Lu (2008). Most of the reported calculations have considered a flapping two-dimensional wing profile. The detailed three dimensional calculations require huge computing resources and several studies of the wing body interference or details about the leading edge vortice have been reported, see e.g., Aono, Liang, and Liu (2008) and Ramamurti and Sandberg (2002). Two-dimensional (2D) simplification is relevant to study the basic mechanisms in flapping flight, see Wang, Birch, and Dickinson (2004).

In this study the CFD software Star-CD (CD-ADAPCO (2006)) was extensively validated prior to the numerical study of the flapping airfoil under ground influence. The numerical solutions reported by Wang (2000a), Wang (2000b) and Wang, Birch, and Dickinson (2004) on forward flapping flight and on dragonfly hovering were used as benchmark test cases to validate the present predictions of the flapping flight.

Next section reports the moving mesh technique developed for the flapping wing. This is followed by the presentation of the results whose first part comprises the validation of the numeric calculations. The second part of the paper comprises the predictions during dragonfly hovering under the ground influence. The paper ends with summary conclusions.

## 2 Numerical Model

### 2.1 Modelling Equations

The frequency of the wing of a flying insect is about $10 - 10^3$ Hz and the Mach number is around $1/300$, and therefore the fluid flow is to be considered incompressible following the Navier-Stokes and continuity equations:

$$\frac{\partial \mathbf{u}}{\partial t} + (\mathbf{u} \cdot \nabla)\mathbf{u} = -\frac{\nabla p}{\rho} + \nu \nabla^2 \mathbf{u}, \tag{1}$$

$$\nabla \cdot \mathbf{u} = 0, \tag{2}$$

with imposed velocity as boundary condition,

$$\mathbf{u}_{bd} = \mathbf{u}_s \tag{3}$$

where the variables stand for $u$ flow field, $p$ pressure, $\rho$ fluid density, $\nu$ kinematic viscosity, $u_{bd}$ velocity at the boundary and $u_s$ velocity at the solid.

To set the characteristic flow regime of this work we can take the example of the dragonfly. The dragonfly has an averaged chord (*c*) of 1 *cm* and a wing tip velocity (*u*) of 1*m/s*, being the correspondent Reynolds number, $Re = \frac{uc}{v}$, of the order of $10^3$. In general, the Reynolds number for insect flight ranges from 10 to $10^4$ which means that the laminar flow assumption should be valid for most of the Reynolds number range.

Although the insect wing is not entirely rigid, most of the computational simulations have considered the wing to be rigid Wang (2000a). This approximation is due to the low level of torsion on the wing and to the difficulty to implement it correctly due to the lack of measurements of the wing behavior under loading throughout the wing stroke. Another complexity arises from the wing interactions, the most evident are the "clap and fling" seen on the butterfly, and the fore and hind-wing interaction seen in dragonfly flight. However, computations of Sun and Lan (2004) showed that the fore-hind wing interaction is weak and can be neglected.

The CFD code Star-CD (CD-ADAPCO (2006)) was selected for this study. The code is based on the finite volume in structured and unstructured meshes employing the PISO (Issa, Gosman, and Watkins (1986)) algorithm. An implicit temporal discretization was selected and different convection discretization treatments, first order upwind and second order Monotone Advection and Reconstruction Scheme (MARS) were compared for different meshes and the MARS scheme was selected.

## 2.2   *Moving Mesh Technique*

High speed photograph (see, e.g. Fry, Sayaman, and Dickinson (2003)) have allowed to fully characterize the insect wing kinematics. The motion of the wing can be divided into translational and rotational phases. The translational phase consists of one downstroke and one upstroke. During the downstroke the wing moves from its rearmost position to its foremost position and the upstrokes describes the return to its original position. The rotational phase occurs at the end of the half-strokes because the wing rotates rapidly and reverses direction for the next half-stroke. During a half-stroke, the wing accelerates rapidly until the middle of the half-stroke, before slowing down on the second part of the half-stroke. The motion of an insect wing can be prescribed relatively to a fixed body by three variables: the position of the tip in spherical coordinates, $(\Theta(t), \Phi(t))$, and the pitching angle $\Psi(t)$, see Fig. 1. This representation is used by some authors but more often the chord positions, of the fore and hind wing are projected onto a two-dimensional slice, showing the so-called *figure-of-eight* kinematics, see e.g. Wang (2005), sketched in Fig. 2.

The simulation of moving bodies can be done without mesh movement for the cases where no relative displacement occurs both, in the body, as well as between any surfaces close to each other. For that, the use of simple body fitted non-inertial

Figure 2: The black sequence corresponds to the downstroke and the grey sequence to the upstroke. This stroke motion is sometimes referred as "figure eight".

reference frames can be appropriate, see, e.g., Wang (2000a) or La Mantia and Dabnichki (2008).

Some other approaches, as Chimera, Liu and Aono (2009), or immersed boundary, Miller and Peskin (2004), use overimposed grids or space regions, respectively, providing that a set of additional conditions were suitably imposed.

Mesh deformations or remeshing are other ways to adjust the discrete space to the moving configuration. This last types were deeply developed and investigated in the field of solid mechanics, and particularly in fracture mechanics where different physical length scales can arise during the simulation, see, e.g., Chung, Choi, and Kim (2003). In the framework of moving finite element methods, Nishioka and Atluri (1980), Nishioka and Takemoto (1989), Nishioka, Tokudome, and Kinoshita (2001), Nishioka, Furutsuka, Tchouikov, and Fujimoto (2002) and Nishioka and Stan (2003) developed many types of moving procedures. Among them, different approaches have been taken, also accordingly to the problem nature. Then the moving elements can be re-defined, usually via Delaunay triangulation, after a renoding or a reconnection process in a given set of nodes, Yamada and Yoshimura (2008) Nishioka, Kobayashi, and Fujimoto (2007).

In the present paper, the wing will be moving during the several strokes and the surrounding mesh has to move with the wing as smoothly as possible. The mesh refinement was achieved by a high density of computational cells near the zone where the flow has higher variations. Several tests were performed to have a good balance between refined and unrefined cells in order to improve numerical accuracy to save computational resources.

The first consideration was to define the dimension of the computational domain. This had to be large enough so it would cause negligible interference on the results. Several tests were conducted to optimize this dimension and it was found that with a computational boundary of 20 chord length for each side of the airfoil the solutions were negligibly influenced from the boundary and therefore throughout this paper this is the dimension to be used, unless stated otherwise.

Zone II of the domain was made circular to provide support to the angular movement. The boundaries of this zone were located far enough from the airfoil, and they accommodate the sliding interface with the outer domain Zone I. Fig. 6 shows the complete computational domain, with zones I, II and III. On Zone III, the mesh was created in order to fit the airfoil geometry. For the elliptical airfoil, it was created an orthogonal elliptical mesh which was very smooth and fitted perfectly the airfoil. It was developed a script to be run on *MATHEMATICA* which created an orthogonal mesh in elliptical coordinates. Fig. 3 shows a detail of the elliptical mesh near the airfoil.
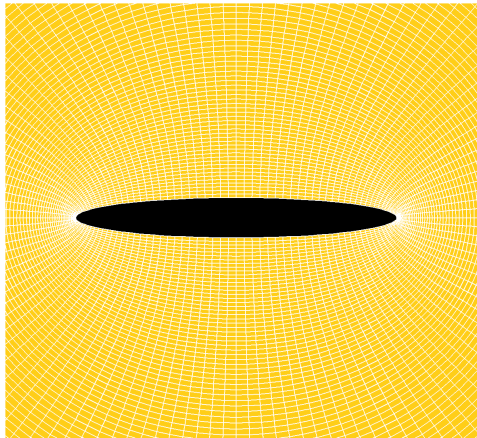


Figure 3: Detail of the elliptical mesh near the airfoil

When the airfoil was represented by a flat plate, the mesh on Zone III had to be adapted to this specific geometry. For this purpose an orthogonal mesh was generated around the flat plate, which provides good results and good computational performance and fits perfectly on the airfoil geometry.

The wing is able to have translational movement on both X and Y axis as well as angular movement to simulate the angles of attack of the wing during the course of the stroke.

For the angular movement the sliding mesh module described in CD-ADAPCO

(2005) was used. This allowed for Zone II and Zone III to rotate inside Zone I, with the boundary cells being attached and detached during the rotation, see Fig. 4.
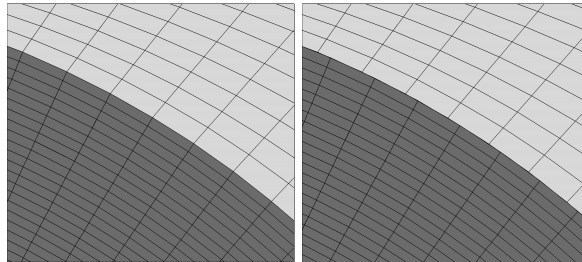


Figure 4: Detail of the sliding interface zone between sub-domains.

For the translational movement the mesh on Zone II had to stretch, to allow Zone III, and the contained airfoil, to move inside this domain. To minimize the flow errors due to grid skewness, only Zone II was allowed to stretch while the geometry of Zone III remained fixed, despite being able to move inside Zone II. The sequence of the moving mesh is illustrated on Fig. 5 with both the stretch and rotation of the mesh.
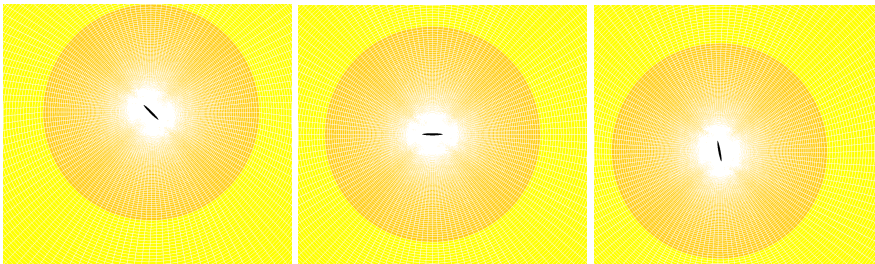


Figure 5: Detail of the moving mesh on the dragonfly hovering problem.

Several meshes were constructed to study the dependence of the solution on the mesh size. The initial mesh comprises 30 thousand computational cells and from there it was refined into meshes of around 100 thousand, 400 thousand and the finner mesh comprising 1.4 million cells, corresponding to a very fine resolution for this 2D problem. To decrease the temporal discretization error the time step was decreased with he spatial mesh refinement and the Courant number, $C = \frac{U \Delta t}{\Delta x}$, was kept small, spite of the used fully implicit method. With the mean Courant number in the order of unity the employed temporal discretization comprised up to 500 time steps per stroke.

The time step ranges from $1.0 \times 10^{-4}$ seconds up to $5.0 \times 10^{-4}$ seconds, requiring a huge number of time steps to solve the problem, the estimated computing time is over 3000 hours in a single processing mode. As such, parallel processing was required in order to achieve a solution within an acceptable time. Star-CD has a subroutine which allows to run automatically in parallel processing but due to the sliding interface it is imperative that this process is defined by the user in order to assure that all the sliding interface remains in the same processor.

The mesh was splited and distributed through the several processors. Each subdomain should have approximately the same number of computational cells, the only exception being the node with the sliding interface. As the processor has to attach and detach those cells, it takes a bit more time to solve each iteration, so the mesh sent to this processor was about 90% of the size of the others to compensate for the delay of the sliding interface .

Also, in order to optimize the parallel computation process, the mesh was *broken* in a way that could minimize the communication between the processors. To achieve this, the contact area between each mesh block and the number of neighbor mesh blocks were minimized. A parallel processing efficiency of around 70% was achieved on 14 processors PC-cluster AMD Opteron.

### 2.3   *Boundary Conditions*

To complete the computational model, a set of appropriated boundary conditions had to be specified in order to simulate a well posed problem.

On the far boundary of Zone I , see Fig. 6, located 20 chords away from the profile a wall no slip boundary condition was specificated (as occurs in the experimental tests) and the total mass of the system remained constant.

For the sliding interface between sub-domains I and II the boundary type was the *attach* (slide related) condition to allow the sub-domains II and III to move freely inside Zone I , as described in the next subsection.

For the implementation of the boundary condition on the airfoil, the process was no so straightforward. From equation 3 we found that the velocity at the boundary is the same as in the solid. Due to the translational and rotational movement of the wing it meant that the velocity is different for each cell of the mesh and is a function of time, where the velocity for each boundary face centroid was prescribed. This velocity was a function of the translational and angular speed, as given by equation:

$$\vec{u_{bd}} = \vec{u_{tr}} + \vec{\omega} \times \vec{r} \tag{4}$$
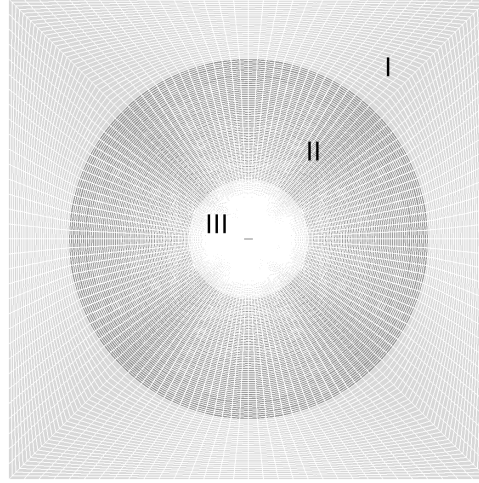
Figure 6: Computational domain, subdivided into three sub-domains.

## 3 Validation Results

### 3.1 Forward Flapping Flight

The forward flapping flight mode is the least complex insect flight mode. It consists on an up and down symmetric movement of the wing, which provides the necessary forces to the forward flight.

We simulate the flapping of a cross section represented by an ellipse with a thickness ratio of $1/8$, as it is usual for this kind of studies. The wing moves forward with a mean flight velocity $U_0$ and flaps with a velocity $U_1(t) = 2\pi f A sin(2\pi f t)$, where $f$ is the flapping frequency and $A$ the flapping amplitude.

For this motion we use three dimensionless quantities: the Reynolds number and the two Strouhal numbers, $St_a$ and $St_c$:

$$Re = U_0 c / \nu \tag{5}$$

$$St_a = f A / U_0 \tag{6}$$

$$St_c = f c / U_0 \tag{7}$$

Where $\nu$ is the kinematic viscosity and $c$ is the wing chord. $St_a$ and $St_c$ indicates the Strouhal numbers based on the flapping amplitude, $St_a$, or chord, $St_c$.

The selected parameters correspond to Wang (2000b) calculations for reference purposes. The Reynolds number was equal to Re=1000. The Strouhal numbers

$St_a = 0.16$ and the flapping frequency was 0.25 and 2Hz, meaning that $St_c = 0.5$ and 4 and the dimensionless time is given by $T_s = tU_0/c$.

On the left boundary of the computational domain, see figure 6, the boundary type corresponds to inlet with velocity $\vec{U}_0$ to simulate the forward velocity. At the top and bottom boundaries slip conditions were employed.

The core section of the mesh was elliptical in order to fit perfectly to the wing geometry. Three meshes were used, around 30000, 100000 and 370000 cells and different flapping frequencies were tested. Results obtained with different meshes showed that the lift coefficient is slightly higher than in Wang (2000b) predictions. As this anomaly was present for all the meshes it appeared that the problem was not from the mesh neither from the used schemes. We concluded that Wang (2000b) post processing didn't account the inertial force into consideration. Fig. 7 presents the results obtained by removing the inertial force from the results obtained with the finer mesh. The inertial force is given by $F_{inert} = \rho A_{ellipsis} a$, where $\rho$ is the air density, $A_{ellipsis}$ is the ellipsis area and $a$ is the acceleration of the wing.
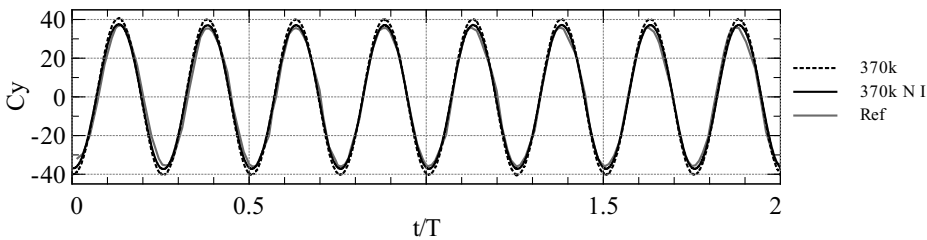


Figure 7: Time dependent lift for a flapping frequency of 2.0Hz.

The predictions are virtual identical to Wang (2000b) results with a sinusoidal temporal evolution for drag and lift coefficients, $C_x$ and the $C_y$, ($C_x$ has a double frequency of $C_y$ because the thrust is generated in both up and down strokes). Fig. 8 shows the results for three meshes and compare them with reference results for flapping frequency of 0.25 $Hz$. We can observe the excellent agreement with the reference data for the lift coefficient. To complete the analysis regarding the force coefficients we have calculated the average $C_x$ and $C_y$ per stroke. The lift coefficient varies symmetrically about the zero mean and therefore the average $C_y$ is zero. The obtained average thrust coefficient $C_x$ per stroke at 0.25Hz was -0.103 and at 2Hz was 0.016. By definition a negative $C_x$ corresponds to a positive thrust in the forward direction, which means that at 2Hz the wing has a negative thrust but while flapping at 0.25Hz the thrust component is positive.

The obtained results were very close to the reference results, Wang (2000b), which

demonstrates the validity of the present analysis.
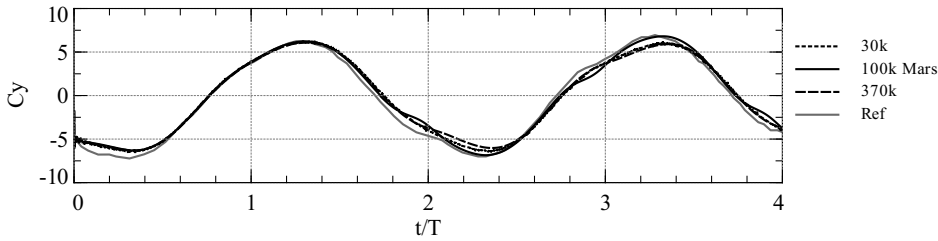


Figure 8: Time dependent lift for a flapping frequency of 0.25Hz.

### 3.2 Dragonfly Hovering

Hovering is a flight mode where the forward velocity is zero and it is very important for insects and MAVs.

For the hovering along an inclined stroke plan, known as the dragonfly hovering, Wang (2000a) introduced a set of equations to model the wing behavior. As for the normal hovering, both the sinusoidal flapping and pitching motion are defined as:

$$x(t) = \frac{A_0}{2}cos(2\pi ft) \tag{8}$$

$$\alpha(t) = \alpha_0 - \alpha_1 sin(2\pi ft + \phi) \tag{9}$$

Fig. 9 shows the foil orientation along a stroke plane inclined at an angle $\beta$.

Through this study the parameters were picked from the dragonfly kinematics analysis Wang (2000a), $A_0 = 2.5cm$, $\phi = 0$, $T = 0.025s$, $c = 1cm$, $\beta = \pi/3$, $\alpha_0 = \pi/4$ and $\alpha_1 = \pi/4$. For comparison purposes, the Reynolds number was 157 and for the remaining analysis the Reynolds number was increased ten times, $Re = 1570$, which is related with the physics of the insect flight.

Fig. 10 shows the predicted vorticity dynamics whose results are in good qualitative agreement with the similar plots displayed by Wang (2000a). On the first two snapshots of Fig. 10 it is shown the generation of a pair of leading and trailing edge vortices of opposite rotation generated by the translational motion. The wing rotation then merges both vortices to form a co-moving dipole pair. On the last two snapshots we see the upstroke phase, where the dipole is separated from the
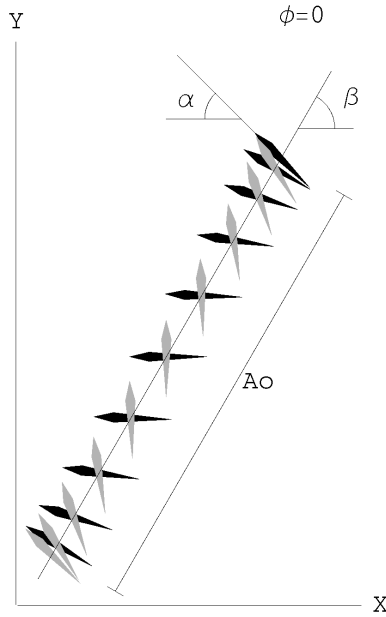
Figure 9: Dragonfly hovering mode.
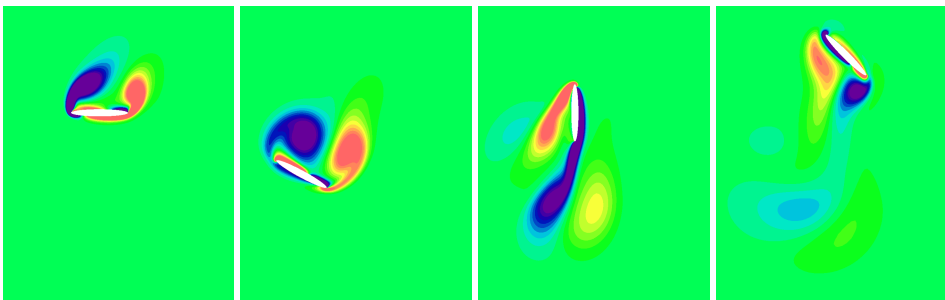


Figure 10: Vorticity field at t/T=0.25, 0.44, 0.74 and 0.99s for Reynolds 157.
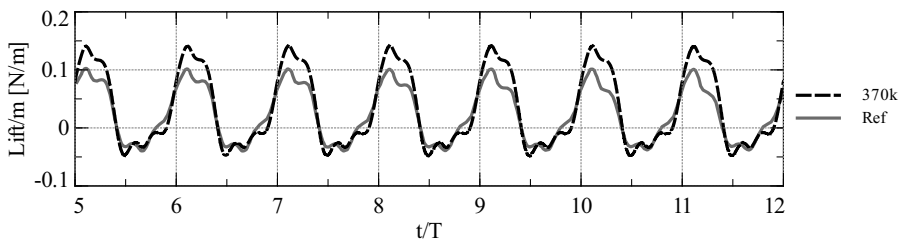


Figure 11: Comparison of lift results for Reynolds 157 with upwind and MARS schemes.
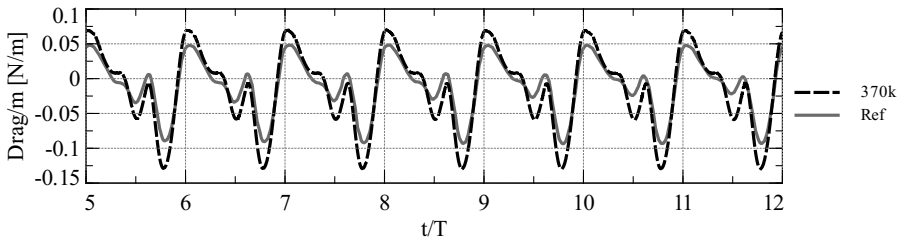
Figure 12: Comparison of drag results for Reynolds 157 with upwind and MARS schemes.

wing and moves downward carrying momentum with it to generate a lift force on the wing. At the end of the stroke the flow sweeps away the vortices generated on the previous cycle, minimizing any interference with the wing on the next cycle. This 2D mechanism of creating and then get rid off the dipole constitutes the fundamental mechanism of hovering flight.

Fig. 11 and Fig. 12 show the predictions obtained for the lift and drag per unit span, using 370000 cells.

Comparing the results obtained for Re=157 with those for Re=1570, and displayed in Fig. 13 and Fig. 14 we notice the increase of the lift peak value, while the drag remained similar to the values obtained with Reynolds number equal to 157 and with higher variations at the end of each half-stroke.
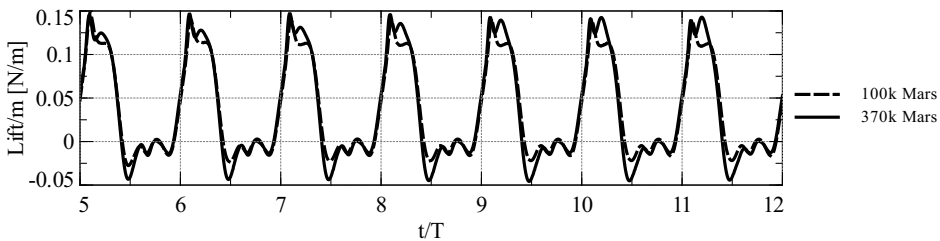


Figure 13: Comparison of lift results for Reynolds 1570 with MARS schemes.

The vorticity field for $Re = 1570$ is similar to the one from Fig. 10 but the vortices are larger than for Reynolds number 157.

The present results show a good comparison with Wang (2000a) results for Re = 157 denoting a good accuracy of the implemented moving mesh technique.
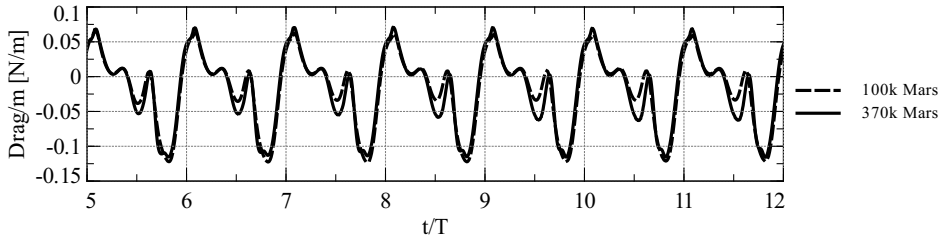
Figure 14: Comparison of drag results for Reynolds 1570 with MARS schemes.

### 3.3 Normal Hovering

During the normal hovering, the wing moves along an horizontal plane. Dickinson, Lehmann, and Sane (1999) made an experimental study of this movement, which was later compared with Wang, Birch, and Dickinson (2004) computational results.

The wing follows a sinusoidal flapping and pitching motion, according to equations 10 and 11, and represented on Fig. 15.

$$x(t) = \frac{A_0}{2}cos(2\pi ft) \tag{10}$$

$$\alpha(t) = \alpha_0 + \alpha_1 sin(2\pi ft + \phi) \tag{11}$$



Figure 15: Normal hovering mode.

For a complete definition of the translational motion two dimensionless parameters were specified. The Reynolds number, $Re = U_{max}c/v = \pi fA_0c/v$, and $A_0/c$. The maximum wing velocity is given by $U_{max}$ and $c$ is the wing chord. During this study the value of $A_0/c$ is set to be 2.8 and the other parameters $\alpha_0$, $\alpha_1$, $\phi$ and $f$ are fixed to be $\pi/2$, $\pi/4$, 0 and 0.25Hz, respectively and Reynolds number 75.

In order to compare the results with the ones obtained by Wang, Birch, and Dickinson (2004), the same normalization, $1/2\rho cU^2$, was used. The dimensionless time scale was obtained by dividing the time by the stroke period.

As for the previous elliptical airfoil, the core section of the mesh was elliptical in order to fit perfectly to the wing geometry. For this analysis it was used a mesh with 370 thousand cells which has already provided good results on previous tests.

Fig. 16 and Fig. 17 compare very satisfactory the present results of the time dependent lift and drag coefficients with Wang, Birch, and Dickinson (2004) reference results. Miller and Peskin (2005) presented numerical results for this case and have also compared with the same reference data. It can be worthmention that the small differences between ours computations and reference results are virtually the same as those obtained by Miller and Peskin (2005).

Excluding the first two strokes, due to the start of the wing movement, the computed forces remain periodic in every stroke. Fig. 17 shows the time dependent drag coefficients, with the drag force in the opposite direction of the movement.
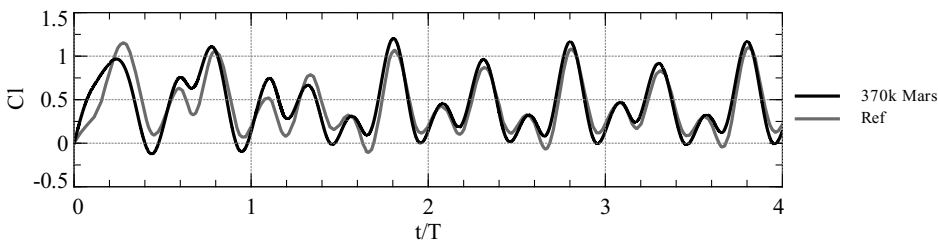


Figure 16: Lift coefficient on normal hovering.
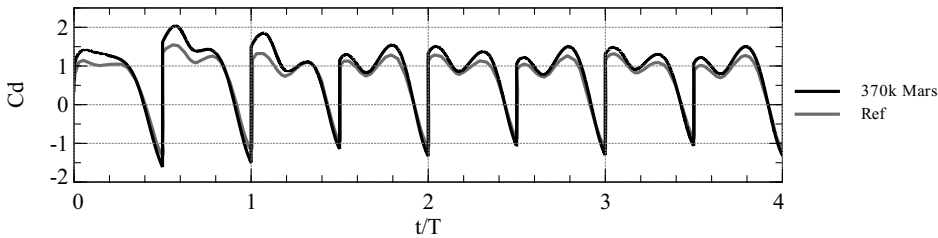


Figure 17: Drag coefficient on normal hovering.

Fig. 18 shows the evolution of the vorticity field for $t/T$=0.15, 0.30, 0.45, 0.60, 0.75 and 0.90s where it is visible the origin of the leading and trailing edge vortices, with the wing creating a dipole and then it being shed by the profile.
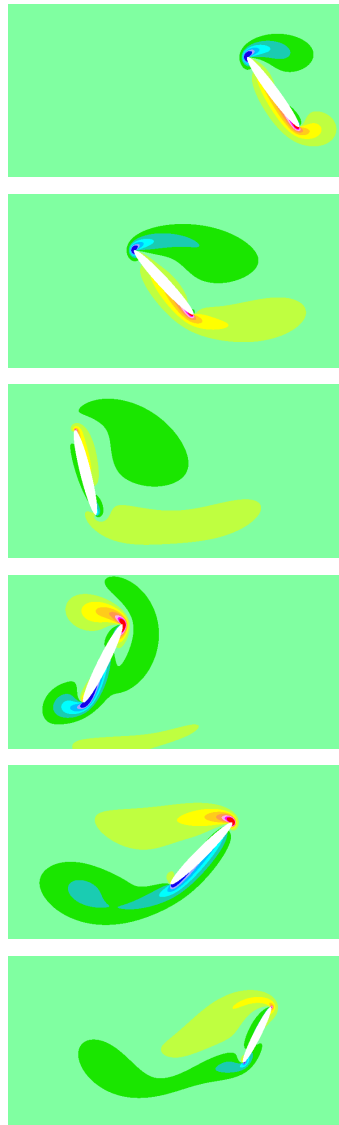
Figure 18: Vorticity field at t/T=0.15, 0.30, 0.45, 0.60, 0.75 and 0.90s.

### 3.3.1   Flat Plate Results

Fig. 19 and Fig. 20 show the comparison of the results obtained for a flat plate and an elliptical airfoil of ratio 1/8. This prediction was made for the dragonfly kinematics with Reynolds number 1570, using a mesh with 100 thousand cells. When comparing both profiles we realize that there is very small differences between the lift and drag coefficients obtained with an elliptical shape airfoil and a flat plate. The reason is due to the LEV, leading edge vortice and the attached vortices that increases lift, being curvature and thickness, for this flapping mode, much less important than it is for example for steady aerodynamics.
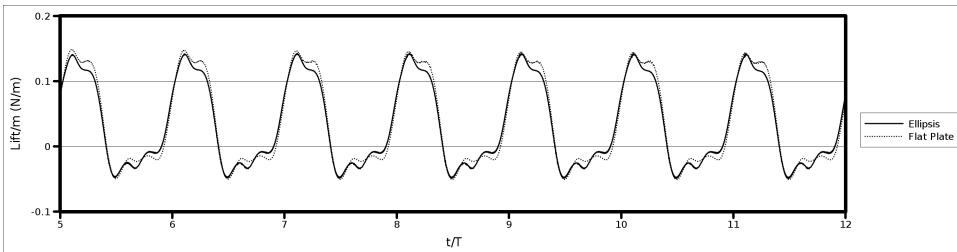


Figure 19: Comparison of lift results obtained with the flat plate and elliptical airfoil.
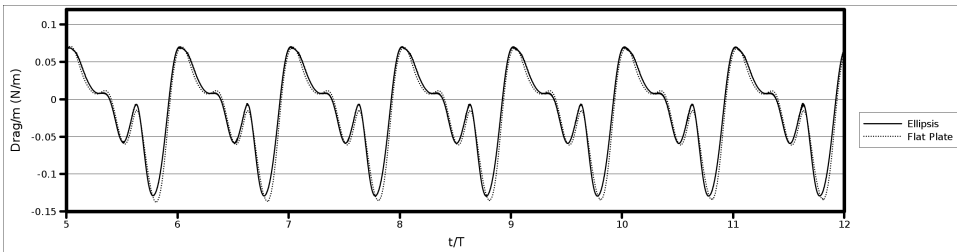


Figure 20: Comparison of drag results obtained with the flat plate and elliptical airfoil.

## 4   Wall Proximity

The ground effect on the dragonfly hovering mode was investigated considering a flat airfoil located at one chord distance, $\frac{h}{c} = 1$, or one and an half chords, $\frac{h}{c} = 1.5$, from the center of the airfoil to the ground, at the downstroke dead point, see figure 21.

The selected kinematic flight parameters correspond to the study presented in the previous sections without the ground effect. The kinematics of the motion are characterized by the amplitude of the translational oscillations of 2.5 chords, stroke plane angle of 60° and the airfoil initial angle of oscillating rotation of $\alpha = 45°$ and the flapping period of $T = 0.025$. We use the chord length of the foil, $c$, and the RMS velocity $U_{rms}$ of the oscillating translation $U_{rms} = 2.22$ as the length and velocity scales respectively. The Reynolds number and the Strouhal number $S_t = fA/U_{rms}$, are equal to $Re = 157$ and $S_t = 0.45$.
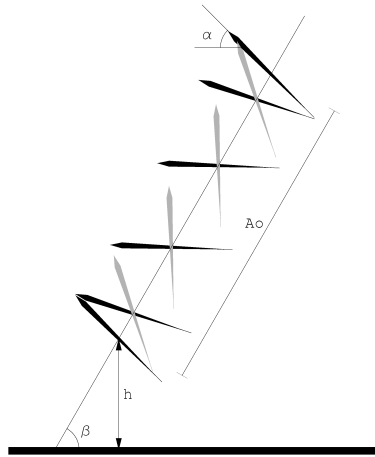


Figure 21: Illustrative sketch of the problem.

The mesh comprises around 250 thousand cells and due to the proximity of the wall, both Zone II and Zone III (see figure 6) of the mesh had to be modified compared with the free flight previous conditions.

Figures 22(a) and 22(b) show the time development of lift and drag forces during 10 stroke periods at $\frac{h}{c} = \infty$, $\frac{h}{c} = 1.5$ and $\frac{h}{c} = 1.0$ for $Re = 157$, 1570 and 3140. Inspection of the figure shows the increase of the drag force in the upstroke, and the variations of the lift are relatively small, indicating that the ground mainly affects the horizontal force. The vertical force is influenced at the vicinity of the downstroke dead point.

Figures 23 and 24 display the lift and drag for the first and after ten strokes.

For $\frac{h}{c} = 1.0$ the $Cl$ was equal to near unity during the first stroke due to the ground effect. However in the subsequent strokes, the lift generation is influenced by the interaction of the vortices with the residual structures with high vorticity from the wake, of the airfoil movement, and from the wall. Relatively to the drag, Cd de-

(a) Lift.



(b) Drag.
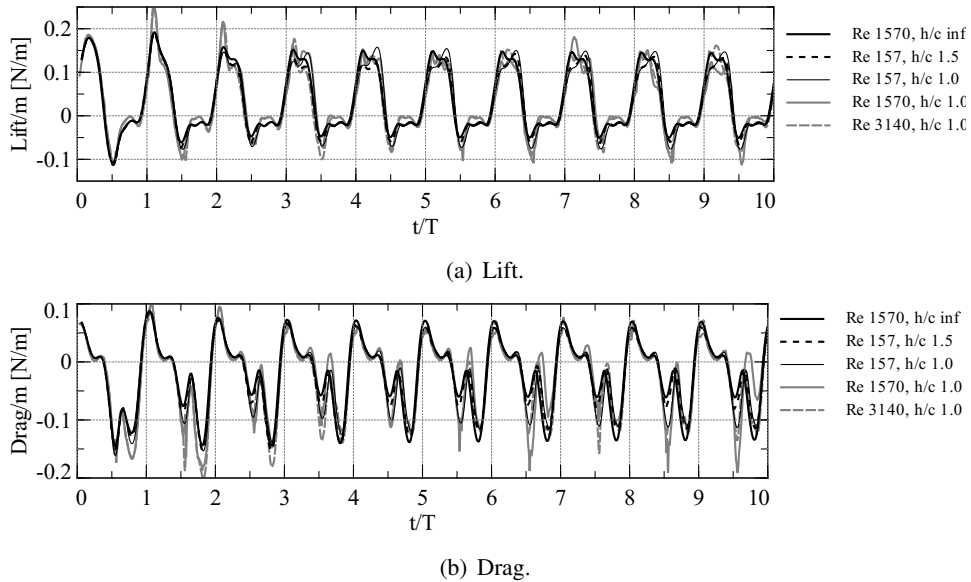
Figure 22: Comparison of lift and drag obtained with Reynolds 157, 1570 and 3140, and different distances from the ground

creases also by the wall influence.

Figure 22 shows that periodic conditions were not obtained. A chaotic temporal evolution is felt and the main responsability is due to the interaction of primary and secondary vortices. One should stress that these secondary vortices are not present during the first stroke, where the airfoil moves impulsively from the rest.

Figure 25 shows the vorticity field for different stroke periods but at the same airfoil position. 10 shows similar conditions without ground influence.

A pair of vortices is generated in the downstroke, the LEV attaches to the foil before the vortices shed when the foil turns upward, and each vortex combines with the one of the opposite sign generated in the upstroke to form two vortex-dipoles, as obtained by Gao and Lu (2008)

When the wing rotates and the vortex is shed, it is observable its impact on the ground and two new vortices are created due to the separation of the wall boundary layer by adverse pressure gradient. In addition the vortices emanating from the wall have grown and tend to surround the vortices that are released from the foil. Increasing then Reynolds number will enhance this interaction because the vortices with opposite vorticity will be stronger.

Hovering is an extreme mode of flight where forward velocity is zero and the high

(a) Lift.



(b) Drag.
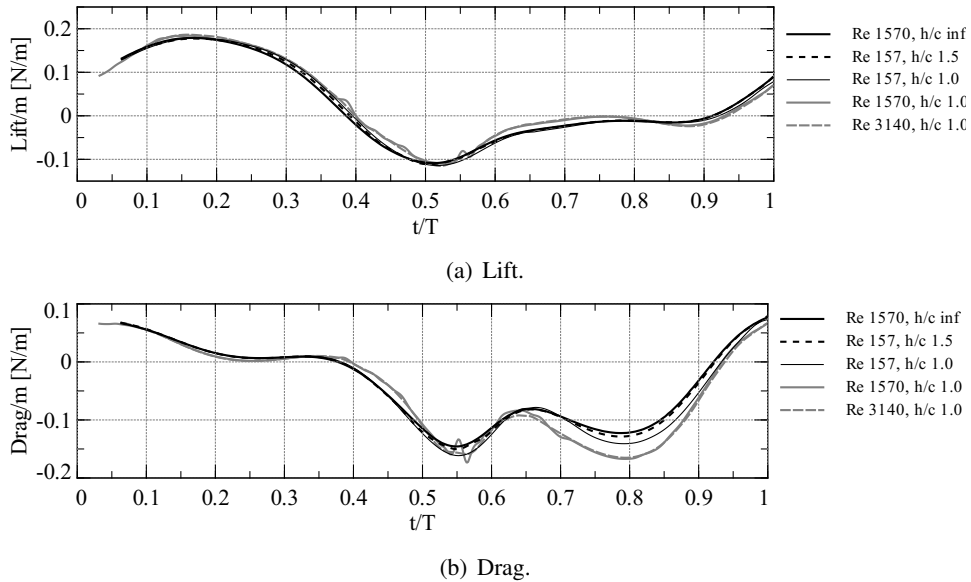
Figure 23: Lift and drag in the tenth stroke

lift required to sustain the animal weight is obtained by drawing air from the ambient and get rid of the vortices to obtain a periodic force. For the set of parameters investigated no periodic force was obtained simply because the pair of vortices that was generated in the downstroke was not completely rid off. Figure 25 shows at stroke period 9 and 10, for example, that the succession of vortex dipoles, that carried the fluid momentum downward and kept an insect loft, were not completely removed. consequently in the next downstroke the interaction of the vortices with the vortical remaining field is very complex and due to Biot-Savart velocity induced a chaotic field may be easily formed.

There are many kinematics that influence drag and lift coefficients, Re, rotation angle, stroke plane angle, airfoil minimum distance to the ground, stroke period, etc. Gao and Lu (2008) investigated the 2D ground effect on insect inclined hovering and a systematic computations for $Re = 100$ show that not only the airfoil to ground distances influences but also the stroke plane inclination angle. The selected set of parameters of $\beta = 60°$, $\alpha = 45°$ and $Re = 157$ are close in agreement with Gao and Lu (2008) parameters of $\beta = 45°$, $\alpha = 60°$ and $Re = 100$. We believe that we add to this flow configuration the information regarding to the non-periodic behavior of the dipole interaction with remaining organized vorticity field.

Figure 26 and 27 shows the evolution of the mean drag and lift forces in each stroke

(a) Lift.



(b) Drag.
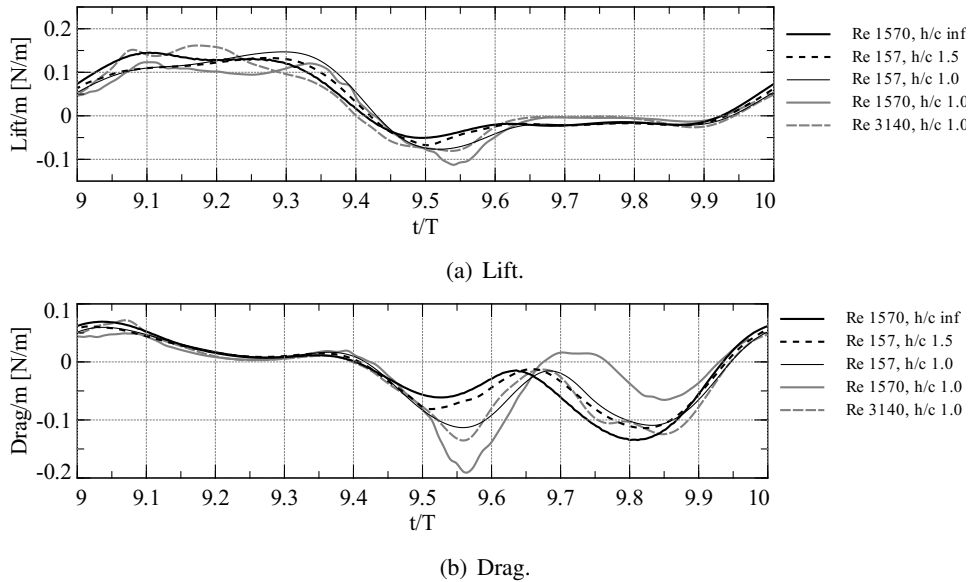
Figure 24: Lift and drag in the first stroke

during the first ten strokes. The oscillations felt with decreasing distance from the ground are a consequence of the "messy remaining vortices" in the stroke path.

## 5 Conclusion

Two-dimensional predictions of a flapping airfoil in inclined hovering flight under ground effect were presented. The numerical predictions were obtained with very fine meshes comprising more that two hundred thousands cells, allowing translational and rotational motion to follow the stroke airfoil motion. The commercial code used was extensively validated with reported predictions for forward and normal and inclined hovering flight modes. Overall the predictions are very satisfactory with the transient evolution of drag and lift forces.

The influence of the ground on the inclined hovering flight of an airfoil, located at a minimum distance of one chord from the ground, displayed with time a nonperiodic set of flow fields. The vortical fields denote the accumulation of previous quadripoles obtained from previous leading and trailing edge vortices and formed ground vortices.

The influence of Reynolds number of 1570, compared with 157 increases the strength of the structures, but the same pattern was observed.

The influence of the hovering inclination angle together with the Strouhal number
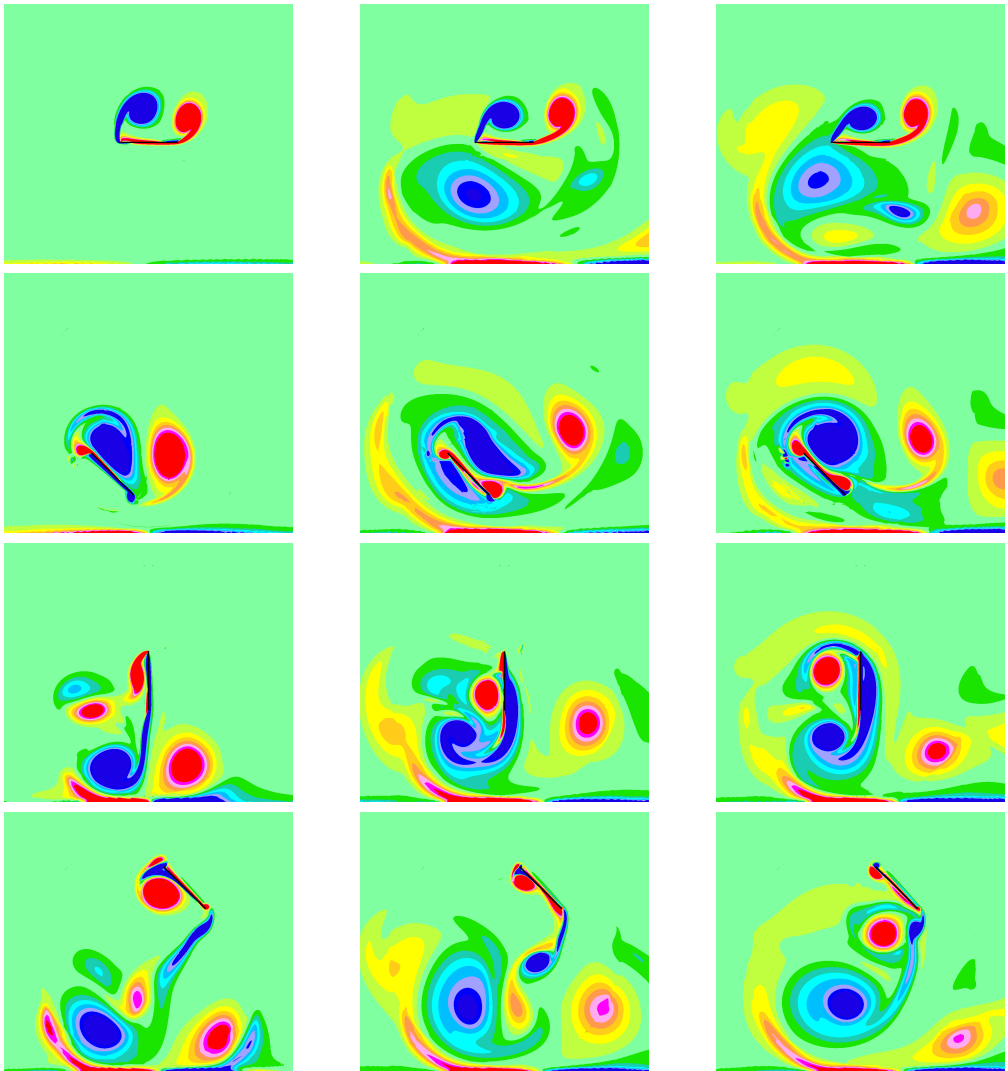
(a) Vorticity field at t/T=0.25, 0.5, 0.75 and 1.0

(b) Vorticity field at t/T=8.25, 8.5, 8.75 and 9.0

(c) Vorticity field at t/T=9.25, 9.5, 9.75 and 10.0

Figure 25: Unsteady development of the ground influence. Vorticity field during the first, the $9^{th}$ and the $10^{th}$ stroke. $\frac{h}{c} = 1.0$. $Re = 1570$.
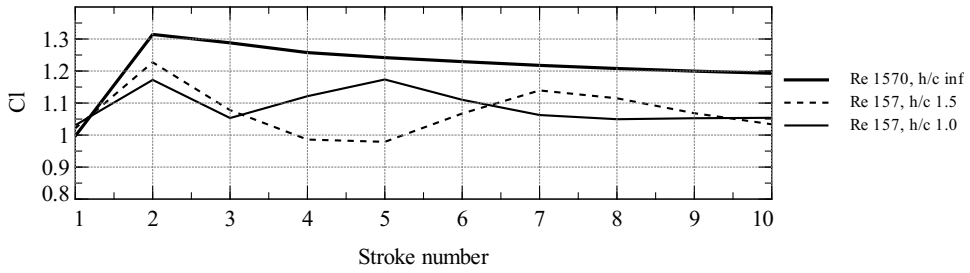
(a) Lift coefficient.
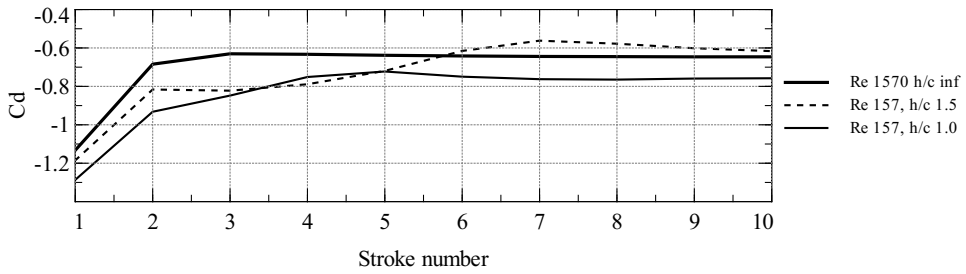


(b) Drag coefficient.

Figure 26: Comparison of lift and drag obtained with Reynolds 157 for different distances.
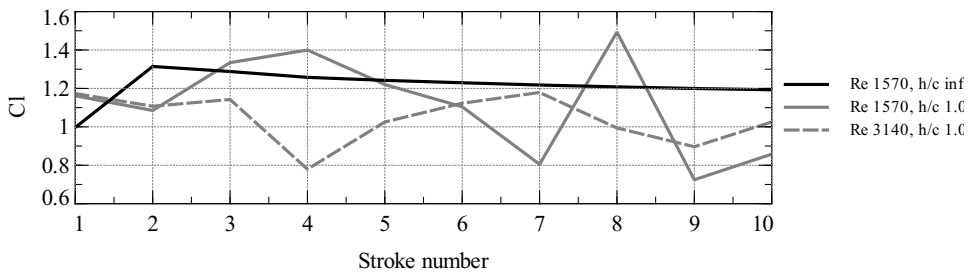


(a) Lift coefficient.
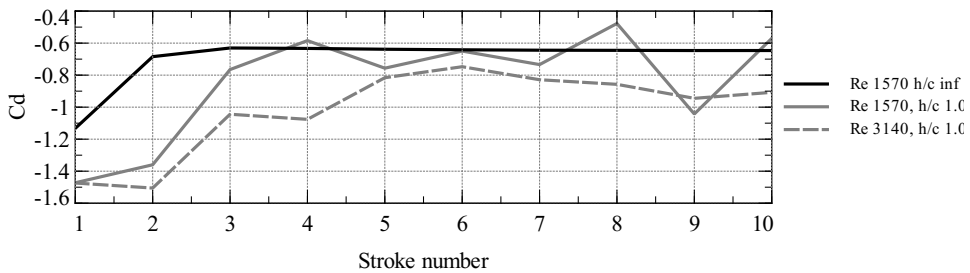


(b) Drag coefficient.

Figure 27: Comparison of lift and drag obtained with Reynolds 1570 and 3140.

deserves further research to fully understand the ground effect influence.

**References**

**Aono, H.; Liang, F.; Liu, H.** (2008):   Near- and far-field aerodynamics in insect hovering flight: an integrated computational study.   *J. Exp. Biol., Vol. 211, pp. 239-257.*

**Birch, J. M.; Dickinson, M. H.** (2001):   Spanwise flow and the attachment of the leading-edge vortex on insect wings.   *Nature, vol. 412, n. 6848, pp. 729-733.*

**CD-ADAPCO** (2005):   Rotating and moving meshes.   *Star-CD Version 3.26 User Guide.*

**CD-ADAPCO** (2006):   Star-cd version 3.26 methodology.

**Chung, S. W.; Choi, Y. J.; Kim, S. J.** (2003):     Computational simulation of localized damage by finite element remeshing based on bubble packing method. *CMES: Computer Modeling in Engineering and Science, Vol. 4, No. 6, pp. 707-718.*

**Dickinson, M. H.; Götz, K. G.** (1993):   Unsteady aerodynamic performance of model wings at low reynolds numbers.   *J. Exp. Biol., Vol. 174, pp. 45-64.*

**Dickinson, M. H.; Lehmann, F. O.; Sane, S. P.** (1999):   Wing rotation and the aerodynamic basis of insect flight.   *Science, Vol. 284, pp. 1954-1960.*

**Eldredge, J. D.** (2005):   Efficient tools for the simulation of flapping wing flows. *43rd AIAA Aerospace Sciences Meeting and Exhibit, Reno, Nevada, U.S.A., 10-13 January.*

**Ellington, C.; van den Berg, C.; Willmott, A.; Thomas, A.** (1996):   Leading-edge vortices in insect flight.   *Nature, 384, pp. 626-630.*

**Ellington, C. P.** (1999):   The novel aerodynamics of insect flight: Applications to micro-air vehicles.   *J. Exp. Biol., Vol. 202, pp. 3439-3448.*

**Fry, S. N.; Sayaman, R.; Dickinson, M. H.** (2003):   The aerodynamic of free-flight manuevers in drosophila.   *Science, 300, pp. 495-498.*

**Gao, T.; Lu, X.** (2008): Insect normal hovering flight in ground effect. *Physics of Fluids, 20, 087101.*

**Ho, S.; Nassef, H.; Pornsinsirirak, N.; Tai, Y. C.; Ho, C. M.** (2003): Unsteady aerodynamics and flow control for flapping wing flyers. *Progress in Aerospace Sciences, Vol. 39, Issue 8, pp. 635-681.*

**Hollick, F. S. J.** (1940): The flight of the dipterous fly muscina stabulans fallén. *Phil. Trans. R. Soc. Lond. B, Vol. 230, n. 572, pp. 357-390.*

**Issa, R.; Gosman, A.; Watkins, A.** (1986): The computation of compressible and incompressible recirculating flows by a non-iterative implicit scheme. *J. Comp. Phys., Vol. 62, 1, pp. 66-82.*

**Jensen, M.** (1956): Biology and physics of locust flight. iii. the aerodynamics of locust flight. *Phil. Trans. R. Soc. Lond. B, Vol. 239, pp. 511-552.*

**La Mantia, M.; Dabnichki, P.** (2008): Unsteady 3d boundary element method for oscillating wing. *CMES: Computer Modeling in Engineering and Science, Vol. 33, 2, pp. 131-153.*

**Lehmann, F.** (2008): When wings touch wakes: understanding locomotor force control by wake-wing interference in insect wings. *J. Exp. Biol., Vol. 211, pp. 224-233.*

**Lighthill, M. J.** (1973): On the weis-fogh mechanism of lift generation. *J. Fluid Mech. 60, part 1, pp. 1-17.*

**Liu, H.; Aono, H.** (2009): Size effects on insect hovering aerodynamics: an integrated computational study. *Bioinsp. Biomim., Vol. 4, 1, 015002 (13pp), doi:10.1088/1748-3182/4/1/015002.*

**Liu, H.; Ellington, C. P.; Kawachi, K.; van den Berg, C.; Willmott, A. P.** (1998): A computational fluid dynamic study of hawkmoth hovering. *J. Exp. Biol., Vol. 201, pp. 461-477.*

**Marey, E. J.** (1868): Determination experimentale du mouvement des ailes des insectes pendant le vol. *C. R. Acad. Sci. Paris, 67, pp. 1341-1345.*

**Maxworthy, T.** (1979): Experiments on the weis-fogh mechanism of lift generation by insects in hovering flight. part 1. dynamics of the 'fling'. *J. Fluid Mech., 93, part 1, pp. 47-63.*

**Miller, L. A.; Peskin, C. S.** (2004): When vortices stick: an aerodynamic transition in tiny insect flight. *J. Exp. Biol., Vol. 207, pp. 3073-3088.*

**Miller, L. A.; Peskin, C. S.** (2005): A computational fluid dynamics of 'clap and fling' in the smallest insects. *J. Exp. Biol., Vol. 208, pp. 195-212.*

**Nachtigall, W.** (1974): Insects in flight. *New York, McGraw-Hill.*

**Nishioka, T.; Atluri, S. N.** (1980): Numerical modeling of dynamic crack propagation in finite bodies by moving singular elements - part i. formulation. *J. App. Mech., Vol. 47, No. 3, pp. 570-576.*

**Nishioka, T.; Furutsuka, J.; Tchouikov, S.; Fujimoto, T.** (2002): Generation-phase simulation of dynamic crack bifurcation phenomenon using moving finite element method based on delaunay automatic triangulation. *CMES: Computer Modeling in Engineering and Science, Vol. 3, No. 1, pp. 129-145.*

**Nishioka, T.; Kobayashi, Y.; Fujimoto, T.** (2007): The moving finite element-method based on delaunay automatic triangulation for fracture path prediction simulations in nonlinear elastic-plasticmaterials. *CMES: Computer Modeling in Engineering and Science, Vol. 17, No. 3, pp. 231-238.*

**Nishioka, T.; Stan, F.** (2003): A hybrid experimental-numerical study on the mechanism of three-dimensional dynamic fracture. *CMES: Computer Modeling in Engineering and Science, Vol. 4, No. 1, pp. 119-139.*

**Nishioka, T.; Takemoto, Y.** (1989): Moving finite element method aided by computerized symbolic manipulation and its application to dynamic fracture simulation. *JSME International Journal, Series I, Vol. 32, No. 3, pp. 403-410.*

**Nishioka, T.; Tokudome, T.; Kinoshita, M.** (2001): Mixed-phase simulation with fracture-path prediction mode using moving finite element method based on delaunay automatic mesh generation. *Int. J. of Solid and Structures, Vol. 38, pp. 5237-5301.*

**Ramamurti, R.; Sandberg, W. C.** (2002): A three-dimensional computational study of the aerodynamic mechanisms of insect flight. *J. Exp. Biol., Vol. 205, pp. 1507-1518.*

**Sane, S. P.** (2003): The aerodynamics of insect flight (review). *J. Exp. Biol., Vol. 206, pp. 4191-4208.*

**Shyy, W.; Berg, M.; Ljungqvist, D.** (1999): Flapping and flexible wings for biological and micro air vehicles. *Progress in Aerospace Sciences, Vol. 35, 5, pp. 455-505.*

**Sun, M.; Lan, S. L.** (2004): A computational study of the aerodynamic forces and power requirements of dragonfly (aeschna juncea) hovering. *J. Exp. Biol., Vol. 207, pp. 1887-1901*.

**Sun, M.; Tang, J.** (2002): Unsteady aerodynamic force generation by a model fruit fly wing in flapping motion. *J. Exp. Biol., Vol. 205, pp. 55-70*.

**Van den Berg, C.; Ellington, C. P.** (1997): The three-dimensional leading-edge vortex of a 'hovering' model hawkmoth. *Phil. Trans. R. Soc. Lond. B, 352, pp. 329-340*.

**Van den Berg, C.; Ellington, C. P.** (1997): The vortex wake of a 'hovering' model hawkmoth. *Phil. Trans. R. Soc. Lond. B, 352, pp. 317-328*.

**Wang, H.; Zeng, L.; Liu, H.; Yin, C.** (2003): Measuring wing kinematics, flight trajectory and body attitude during forward flight and turning maneuvers in dragonflies. *J. Exp. Biol., Vol. 206, pp. 745-757*.

**Wang, Z. J.** (2000): Two dimensional mechanism for insect hovering. *Phys. Rev. Lett., Vol. 85, n. 10, pp. 2216-2219*.

**Wang, Z. J.** (2000): Vortex shedding and frequency selection in flapping flight. *J. Fluid Mech., Vol. 410, pp. 323-341*.

**Wang, Z. J.** (2005): Dissecting insect flight. *Annu. Rev. Fluid Mech., 37, pp. 183-210*.

**Wang, Z. J.; Birch, J. M.; Dickinson, M. H.** (2004): Unsteady forces and flows in low reynolds number hovering flight: two-dimensional computations *vs* robotic wing experiments. *J. Exp. Biol., Vol. 207, pp. 449-460*.

**Weis-Fogh, T.** (1973): Quick estimates of flight fitness in hovering animals, including novel mechanisms for lift production. *J. Exp. Biol., Vol. 59, 169-230*.

**Yamada, T.; Yoshimura, S.** (2008): Line search partitioned approach for fluid-structure interaction analysis of flapping wing. *CMES: Computer Modeling in Engineering and Science, Vol. 24, 1, pp. 51-60*.